Euler and Navier-Stokes Solutions for Flow over a Conical Delta Wing

Richard W. Newsome*
NASA Langley Research Center, Hampton, Virginia

The simulation of vortical flow about a conical delta wing (14:1 elliptic cone) by the Euler equations is studied. Navier-Stokes solutions are generated for comparison with the inviscid results. At the flight condition considered, the viscous solutions reveal a large primary leading-edge separation vortex and a smaller secondary vortex. The viscous solutions are shown to be grid-resolved. On a coarse grid, the Euler solutions result in a primary separation vortex but no secondary vortex. A comparison of pressure coefficient with the viscous solution shows surprising agreement. The agreement is, unfortunately, fortuitous. When the Euler equations are solved on the fine, viscous grid, the large separation vortex is eliminated. Instead, a cross-flow shock appears. Shock curvature introduces sufficient vorticity to produce a small vortex downstream of the shock. This inviscid result, fundamentally different from the viscous case, is a valid solution to the Euler equations. The coarse-grid Euler solution is characterized by the production of spurious vorticity and entropy due to numerical error at the leading edge. It is neither a valid solution to the Euler equations nor a reliable approximation to the real viscous flow. The use of a Kutta condition is investigated for both the fine- and coarse-grid Euler solutions. It is shown that the Kutta condition fails to produce a grid-independent simulation of the actual viscous flow.

Introduction

RECENTLY, much attention has been devoted to the numerical simulation of flow about swept delta wings at moderate to high angles of attack. For subsonic leading edges that are sharp or of a small radius of curvature, the flow separates at the tips and forms two counterrotating vortices on the leeward wing surface. The presence of the vortices produces a pressure minimum on the upper surface and results in an additional lift component not predicted by linear theory.

Approximate methods of predicting vortex lift include Polhamus'[1] "leading-edge-suction analogy" and a number of panel methods[2] that model the free vortex sheet and the size and shape of the vortices. The suction analogy does not furnish any flowfield information, while the panel methods are complicated and restricted to simple shapes at subsonic speeds.

Emphasis currently has shifted to methods based on more fundamental principles. The Reynolds-averaged, Navier-Stokes equations model all physical mechanisms and provide the most accurate results. Vigneron et al.[3] solved the conical and parabolic approximations to the Navier-Stokes equations for vortical flow about a sharp-edged delta wing. Fujii and Kutler[4,5] solved the three-dimensional Navier-Stokes equations to compute the leading-edge separation about a swept wing with rounded edges. Rizzetta and Shang[6] recently presented three-dimensional Navier-Stokes solutions for a delta wing with sharp edges. The principal drawbacks of Navier-Stokes solutions are the high computational costs necessary for viscous resolution and the need to model the turbulence in an approximate manner.

As a less expensive alternative to the Navier-Stokes equations, the Euler equations offer many attractive features. In contrast to potential methods, the Euler equations provide the correct Rankine-Hugoniot shock jump conditions. They also allow for rotational effects through the transport of vorticity. The conservative finite volume Runge-Kutta code developed by Jameson et al.[7] has proven quite popular in calculating Euler solutions for wings and wing-bodies. The computed solutions produce the correct lift without explicitly imposing a Kutta condition. Numerous computations[8-11] for flow about swept delta wings with both sharp and rounded leading edges also reveal the characteristic leading-edge separation vortex. Since flow separation is usually associated with the generation of vorticity through the no-slip boundary condition in a viscous flow, its occurrence in an inviscid solution is of great interest.

Conditions necessary for flow separation include the presence of vorticity in the flow as well as an adverse pressure gradient. Both conditions may be met in a purely inviscid flow, but only for very specific circumstances. In accord with Crocco's theorem, the Euler equations allow for the generation of vorticity through nonconstant shock strength (shock curvature, shock intersection, etc.). Salas[12] first demonstrated shock-induced inviscid separation for the transonic flow about a cylinder. Marconi[13] published similar results for supersonic flow about a circular cone. Rizzi[14] has postulated that the vorticity necessary for flow separation may be generated by the transient appearance of a shock as the flow expands around a wing leading (or trailing) edge. The shock then disappears in the steady state. It is also known that inviscid separation may be produced strictly through numerical means.[15]

The purpose of the present effort is to study solutions to the Euler and Navier-Stokes equations for flow about a delta wing with rounded edges of small curvature radius. In the limit of infinite tip sharpness, incompressible inviscid flow expands to infinite velocity while compressible inviscid flow expands to the limit of vacuum pressure. Since neither of these possibilities is physically realizable in a viscous gas, the flow must separate at the salient edge. Once separation is established at the wingtip, the Euler equations correctly describe the transport of vorticity and entropy from the origin at the leading edge, along the feeding sheet to the roll-up into the leeward surface vortex. As the radius of curvature approaches zero for a rounded edge, Navier-Stokes solutions would be expected to result in a leading-edge separation well before the inviscid expansion limit is realized.

Received Dec. 24, 1984; presented as Paper 85-0111 at the AIAA 23rd Aerospace Sciences Meeting, Reno, NV, Jan. 14-17, 1985; revision received Aug. 1, 1985. This paper is declared a work of the U.S. Government and is not subject to copyright protection in the United States.

*Major, USAF; Air Force Wright Aeronautical Laboratories, Air Force Systems Command Liaison Office. Member AIAA.

This situation is quite challenging, however, for an Euler code. Valid Euler solutions must approach the inviscid expansion limit. In practice numerical solutions to the Euler equations, under these conditions, often result in inviscid separation. There are several known sources of numerical error that result in viscous-like terms. Shock-capturing algorithms require the addition of artificial damping to control shock oscillations. Such terms are dissipative and also significant in regions of rapid expansion. The numerical algorithm is itself necessarily dissipative for stability reasons. The implementation of body surface boundary conditions is another possible source of error. The result of such effects on the Euler solutions will be assessed. Two questions are of primary importance:

1) Are the solutions valid in the sense that vorticity and entropy are introduced in a manner consistent with inviscid flow?

2) If the origin of the vorticity/entropy is numerical, are the solutions nevertheless a consistent and reliable approximation to the real viscous flow?

Solution Method

If interest is restricted to the study of supersonic flow past conical bodies, then the governing equations may be simplified since the resulting flow will also be conical. A conical flow has the property that all flow quantities are invariant on rays that pass through the apex of the conical surface. All derivatives in the conical direction may then be neglected, reducing the number of spatial dimensions by 1. The conical equations may be obtained by introduction of conical variables:

$$x=\tilde{x}, \quad y=\tilde{y}/\tilde{x}, \quad z=\tilde{z}/\tilde{x} \tag{1}$$

into the three-dimensional Navier-Stokes equations, written in the Cartesian variables $(\tilde{x},\tilde{y},\tilde{z})$. Upon simplification for conical flow, the equations are then transformed into a uniform computational plane through the numerically evaluated transformation

$$\zeta=\zeta(\tilde{x},\tilde{y},\tilde{z})=\zeta(y,z), \quad \eta=\eta(\tilde{x},\tilde{y},\tilde{z})=\eta(y,z)$$

The equations may be written in nondimensional form as

$$\frac{\partial}{\partial t}\left(\frac{1}{J}U\right)+\frac{\partial}{\partial\zeta}\left(\frac{1}{J}[G-G_v]\right)$$
$$+\frac{\partial}{\partial\eta}\left(\frac{1}{J}[H-H_v]\right)+\frac{1}{J}[Q-Q_v]=0 \tag{2}$$

where

$$U=\begin{bmatrix}\rho\\ \rho u\\ \rho v\\ \rho w\\ \rho E\end{bmatrix}, \quad G=\begin{bmatrix}\rho V\\ \rho uV+\zeta_x p\\ \rho vV+\zeta_y p\\ \rho wV+\zeta_z p\\ [\rho E+p]V\end{bmatrix}$$

$$H=\begin{bmatrix}\rho W\\ \rho uW+\eta_x p\\ \rho vW+\eta_y p\\ \rho wW+\eta_z p\\ [\rho E+p]W\end{bmatrix}, \quad Q=2\begin{bmatrix}\rho u\\ \rho u^2+p\\ \rho uv\\ \rho uw\\ [\rho E+p]u\end{bmatrix}$$

$$E=e_I+\tfrac{1}{2}(u^2+v^2+w^2)$$

$$V=\zeta_x u+\zeta_y v+\zeta_z w, \quad W=\eta_x u+\eta_y v+\eta_z w$$

In Eq. (2), transformation derivatives with respect to $(\tilde{x},\tilde{y},\tilde{z})$ are defined in terms of the simpler two-dimensional transformation with respect to the conical variables, (y,z), as

$$(\zeta_{\tilde{y}},\zeta_{\tilde{z}},\eta_{\tilde{y}},\eta_{\tilde{z}})=\frac{1}{\tilde{x}}(\zeta_y,\zeta_z,\eta_y,\eta_z)$$

where

$$\zeta_y=\frac{z_\eta}{J^{-1}}, \quad \zeta_z=\frac{-y_\eta}{J^{-1}}$$

$$\eta_y=\frac{-z_\zeta}{J^{-1}}, \quad \eta_z=\frac{y_\zeta}{J^{-1}}$$

$$J=[\zeta_y\eta_z-\zeta_z\eta_y]=[y_\zeta z_\eta-y_\eta z_\zeta]^{-1}$$

Similarly, it is convenient to define

$$\zeta_x=-[y\zeta_y+z\zeta_z], \quad \eta_x=-[y\eta_y+z\eta_z]$$

The term, $1/\tilde{x}$, is then absorbed in the nondimensionalization. This viscous terms are

$$G_v=\begin{bmatrix}0\\ \zeta_x\tau_{xx}+\zeta_y\tau_{xy}+\zeta_z\tau_{xz}\\ \zeta_x\tau_{xy}+\zeta_y\tau_{yy}+\zeta_z\tau_{yz}\\ \zeta_x\tau_{xz}+\zeta_y\tau_{yz}+\zeta_z\tau_{zz}\\ \zeta_x b_x+\zeta_y b_y+\zeta_z b_z\end{bmatrix}$$

$$H_v=\begin{bmatrix}0\\ \eta_x\tau_{xx}+\eta_y\tau_{xy}+\eta_z\tau_{xz}\\ \eta_x\tau_{xy}+\eta_y\tau_{yy}+\eta_z\tau_{yz}\\ \eta_x\tau_{xz}+\eta_y\tau_{yz}+\eta_z\tau_{zz}\\ \eta_x b_x+\eta_y b_y+\eta_z b_z\end{bmatrix}$$

$$Q_v=\begin{bmatrix}0\\ \tau_{xx}\\ \tau_{xy}\\ \tau_{xz}\\ b_x\end{bmatrix}$$

$$\tau_{xx}=\frac{1}{Re_x}[2\mu u_x+\lambda\Phi], \quad \tau_{yy}=\frac{1}{Re_x}[2\mu v_y+\lambda\Phi],$$

$$\tau_{zz}=\frac{1}{Re_x}[2\mu w_z+\lambda\Phi]$$

$$\tau_{xy}=\frac{\mu}{Re_x}[u_y+v_x], \quad \tau_{xz}=\frac{\mu}{Re_x}[u_z+w_x],$$

$$\tau_{yz}=\frac{\mu}{Re_x}[v_z+w_y]$$

$$b_x=u\tau_{xx}+v\tau_{xy}+w\tau_{xz}-q_x, \quad b_y=u\tau_{xy}+v\tau_{yy}+w\tau_{yz}-q_y$$

$$b_z=u\tau_{xz}+v\tau_{yz}+w\tau_{zz}-q_z$$

$$q_x = -\frac{\mu\gamma}{Re_x P_R} e_{Ix}, \; q_y = -\frac{\mu\gamma}{Re_x P_R} e_{Iy}, \; q_z = -\frac{\mu\gamma}{Re_x P_R} e_{Iz}$$

$$\Phi = (u_x + v_y + w_z), \; \lambda = -\tfrac{2}{3}\mu, \; \mu = \left(\frac{T}{T_0}\right)^{3/2} \left(\frac{T_0 + S_0}{T + S_0}\right)$$

$$P_R = 0.72, \qquad Re_x = \frac{\rho_{T_\infty} u_{\max} \tilde{x}}{\mu_0}$$

The nondimensionalization is given as

$$u = \frac{\tilde{u}}{u_{\max}}, \quad v = \frac{\tilde{v}}{u_{\max}}, \quad w = \frac{\tilde{w}}{u_{\max}},$$

$$u_{\max} = \sqrt{2\tilde{H}_{T_\infty}}, \quad \rho = \frac{\tilde{\rho}}{\rho_{T_\infty}}, \quad p = \frac{\tilde{p}}{\rho_{T_\infty} u_{\max}^2},$$

$$T = \frac{\tilde{T}}{T_{T_\infty}}, \quad E = \frac{\tilde{E}}{u_{\max}^2}, \quad H = \frac{\tilde{H}}{u_{\max}^2},$$

$$t = \frac{\tilde{t}}{\tilde{x}/u_{\max}}, \quad \mu = \frac{\tilde{\mu}}{\mu_0}$$

where ($\tilde{}$) denotes a dimensional variable.

The conical assumption is exact for inviscid flow. For viscous flow, a length-scale dependence remains and is contained in the Reynolds number. The flow may be thought of as "locally conical" with the Reynolds number determining the location of the conical plane in which the solution is obtained. The validity of this approximation has been well established through experiment and computation.[16,17] The Reynolds number is restricted to values for which the flow would be expected to remain laminar.

The governing equations are marched in time to an assumed steady state from a prescribed initial condition. MacCormack's unsplit, explicit, finite difference algorithm[18] was used to obtain numerical solutions. The method is second-order accurate in space and time and conditionally stable. Provision was made to advance the solution at the local stability limit up to a maximum of some multiple of the global minimum time step. To control shock oscillations, MacCormack's[19] pressure damping was incorporated into the scheme.

It is useful to illustrate sources of numerical dissipation in the algorithm by a simple example problem. The one-dimensional Euler equations in nonconservative form are

$$u_t + A u_x = 0 \tag{3}$$

If the A matrix is assumed constant, the equations may be written in diagonal form as

$$w_t + \lambda w_x = 0 \tag{4}$$

where

$$w = T^{-1} u \text{ and } \lambda = T^{-1} A T$$

Warming and Hyett[20] derived the modified equation for the Lax-Wendroff algorithm applied to Eq. (3). For the linear equation, the MacCormack scheme is identical to the Lax-Wendroff scheme and the modified equation is given as

$$w_t + \lambda w_x = -\frac{\lambda}{6} (\Delta x^2 - \lambda^2 \Delta t^2) w_{xxx}$$
$$- \frac{\lambda^2 \Delta t}{8} (\Delta x^2 - \lambda^2 \Delta t^2) w_{xxxx} + \ldots \tag{5}$$

The effect of the pressure damping is to add an additional term of Eq. (5) of the form

$$\epsilon \Delta x^3 \left(\frac{|\lambda_{\max}|}{4p} |p_{xx}| w_x \right)_x$$

Even derivatives of w are dissipative while odd derivatives are dispersive. Thus, it can be seen that dissipation is introduced both by the algorithm and the artificial damping necessary for control of shock oscillations. It should be noted, however, that the leading truncation error term is dispersive and its effects may predominate when the flow gradients are poorly resolved.

Initial conditions correspond to an impulsive entry of the body into the undisturbed freestream flow. Since all shocks are to be captured, the grid is extended beyond the bow shock so that freestream conditions may be prescribed on the outer boundary. Along the centerline of the wing, a symmetry condition is applied through reflection. On the body surface, for viscous flow, the no-slip condition is applied. An adiabatic wall boundary condition provides surface temperature and the normal momentum equation gives surface pressure.

$$(u,v,w) = 0$$
$$(\nabla T \cdot \hat{N}_s) = 0 \rightarrow T_s \text{ or } T_s \text{ specified}$$
$$(\nabla P \cdot \hat{N}_s) \approx 0 \rightarrow P_s \tag{6}$$

The inviscid surface boundary condition is more difficult. The tangency condition provides one boundary condition for velocity.

$$(u,v,w) \cdot \hat{N}_s = 0 \tag{7}$$

In the steady state, total enthalpy,

$$H_{T_\infty} = \frac{\gamma}{\gamma - 1} \frac{P}{\rho} + \tfrac{1}{2} V_m{}^2 \tag{8}$$

is constant and this condition may be prescribed in the transient as well. The projection of the nonconservative momentum equation along the surface normal, $\hat{N}_s$, again provides an equation for surface pressure, P_s, which involves centripetal acceleration terms due to nonzero surface velocities. To completely specify the surface conditions, the orientation, $\hat{N}_t$, and magnitude, V_m, of the surface tangent plane velocity vector must be specified. Alternatively, a thermodynamic variable may be prescribed rather than V_m.

Two different approaches were taken to establish the latter two boundary conditions. A simple and often-used choice is to extrapolate the tangent plane velocity vector from neighboring interior points. This boundary condition is not accurate unless the surface curvature is small. Best results were obtained with a method developed by Abbett.[21] The governing equations are solved on the surface using a forward difference procedure corrected to second-order accuracy. Although the resulting velocity vector does not satisfy tangency, its projection on the tangent plane provides the orientation of the final velocity vector, $\hat{N}_t$. The computed pressure is corrected to a value consistent with a rotation of the velocity vector to satisfy the tangency condition

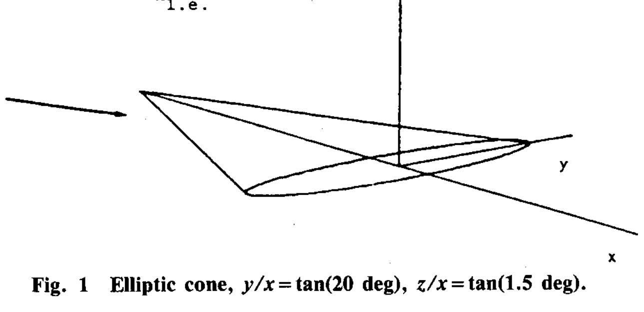

Fig. 1 Elliptic cone, $y/x = \tan(20\text{ deg})$, $z/x = \tan(1.5\text{ deg})$.

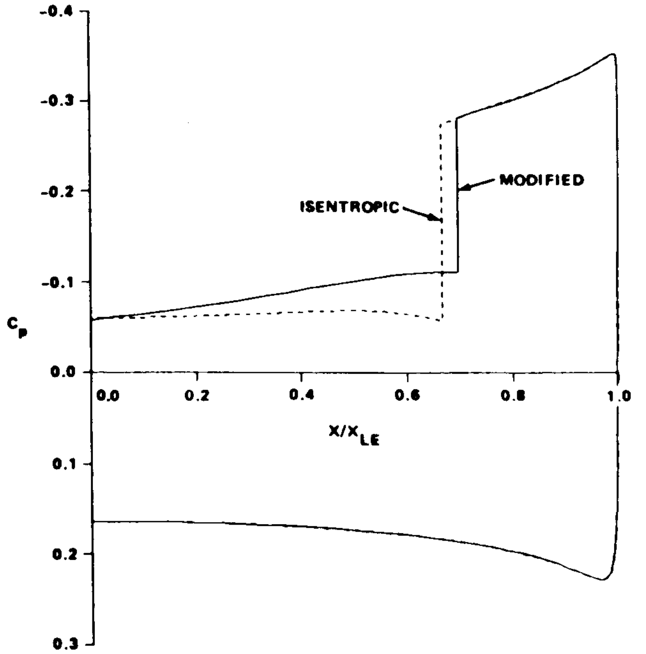

Fig. 2 Pressure coefficient, potential and modified potential equations.[24]

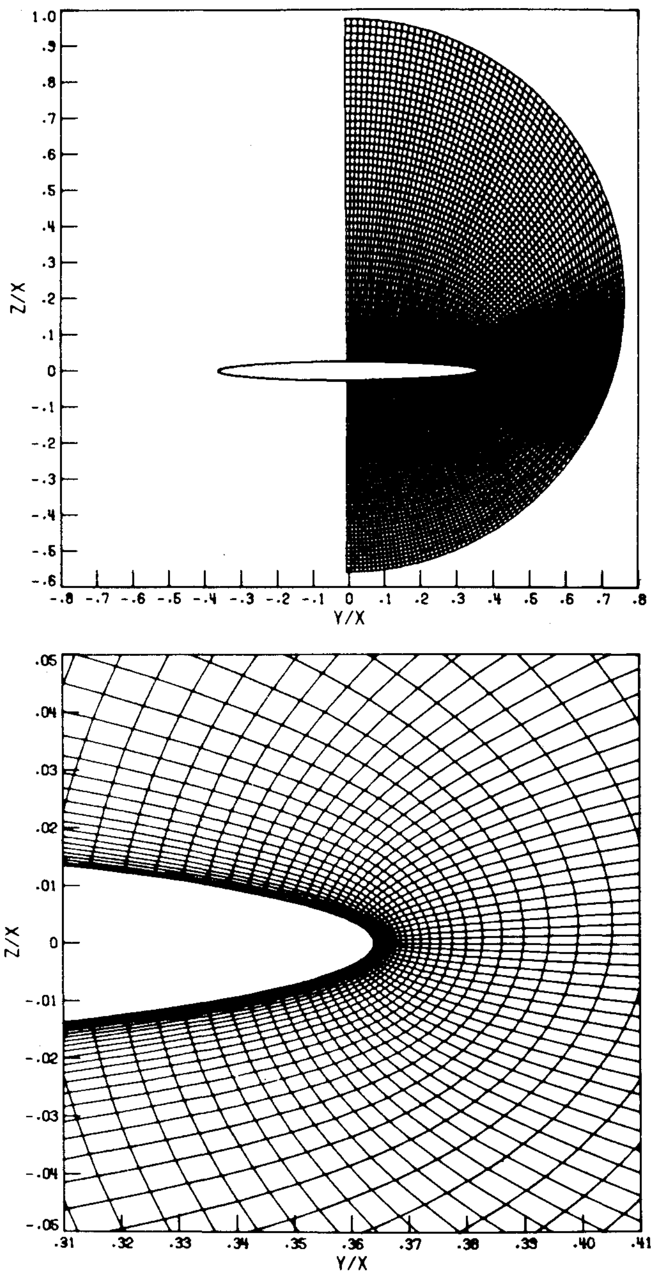

Fig. 3 Fine-grid (151×65) points.

through a Prandtl-Meyer expansion or compression. The resulting pressure is nearly identical with that given by the normal momentum equation. The specification of the entropy on the surface, together with constant total enthalpy, Eq. (8), then gives the magnitude of the velocity vector, V_m. The Abbett procedure provides results consistent with the overall second-order accuracy of the numerical scheme.

Results

A thin elliptic cone, Fig. 1, with half-angles 20 and 1.5 deg in the lateral and vertical directions was chosen for study. This particular geometry provides a realistic approximation to a sharp leading edge while maintaining a continuous curvature in the tip region. The flow condition for all cases considered was Mach 2 at 10-deg angle of attack.

Solutions to the potential equation for this geometry have been computed by several authors.[22,23] Even if the leading edge is poorly resolved, the expansion must be isentropic. For this reason, the potential solution provides a valuable comparison with the Euler solutions. The potential flow calculation displays a rapid expansion about the leading edge to a pressure very close to the vacuum limit ($C_{p_{\text{lim}}} = -0.357$). The supersonic crossflow on the leeward surface is terminated by a strong cross-flow shock. The cross-flow shock strength is outside the range of validity for an isentropic shock; Siclari and Rubel[24] have shown that better results may be obtained by fitting Rankine-Hugoniot shock jumps instead of isentropic jump conditions. A plot of the pressure coefficient for the potential and "modified potential" results is shown in Fig. 2.

Navier-Stokes Solution

Calculations were made on two different grids at a Reynolds number of $Re_\infty = \rho_\infty u_\infty x/\mu_\infty = 0.1 \times 10^6$. The first grid consisted of 65 radial and 121 circumferential (65×121) points with an equal minimum step size in both directions, $\Delta s/x = 0.0006$, at the tip. This radial step size was maintained around the body. A second grid contained (65×151) points with finer clustering such that an equal minimum step size again was set at the tip with a value of $\Delta s/x = 0.0002$. This radial step size was relaxed away from the tip to the previous value, $\Delta s/x = 0.0006$. Both grids were exponentially clustered in the tip region in the two coordinate directions. The finer grid and an enlarged view of the tip region are shown in Fig. 3.

The convergence criterion was taken to be a three-order-of-magnitude reduction in the Euclidean norm of the residual of the conservative variables over the grid for all calculations. At a Reynolds number of 0.1×10^6, the windward symmetry plane boundary layer contained 14 grid points and the leading-edge boundary layer contained 7 points on the finer grid. The cross-flow velocity plot is shown in Fig. 4 where the cross-flow velocity is defined as the Cartesian components of the velocity vector

$$\vec{V}_{\text{C.F.}} = \vec{V} - |\vec{V}|\hat{e}_r \qquad \hat{e}_r = (\hat{i} + y\hat{j} + z\hat{k})/\sqrt{1 + y^2 + z^2}$$

in the y,z plane. The flow separated at the leading edge with a large primary vortex and a smaller secondary vortex. A comparison of the solutions on the two grids revealed nearly identical results; thus, the flow is grid-resolved. A solution at a Reynolds number 0.5×10^6 was also computed on the finer

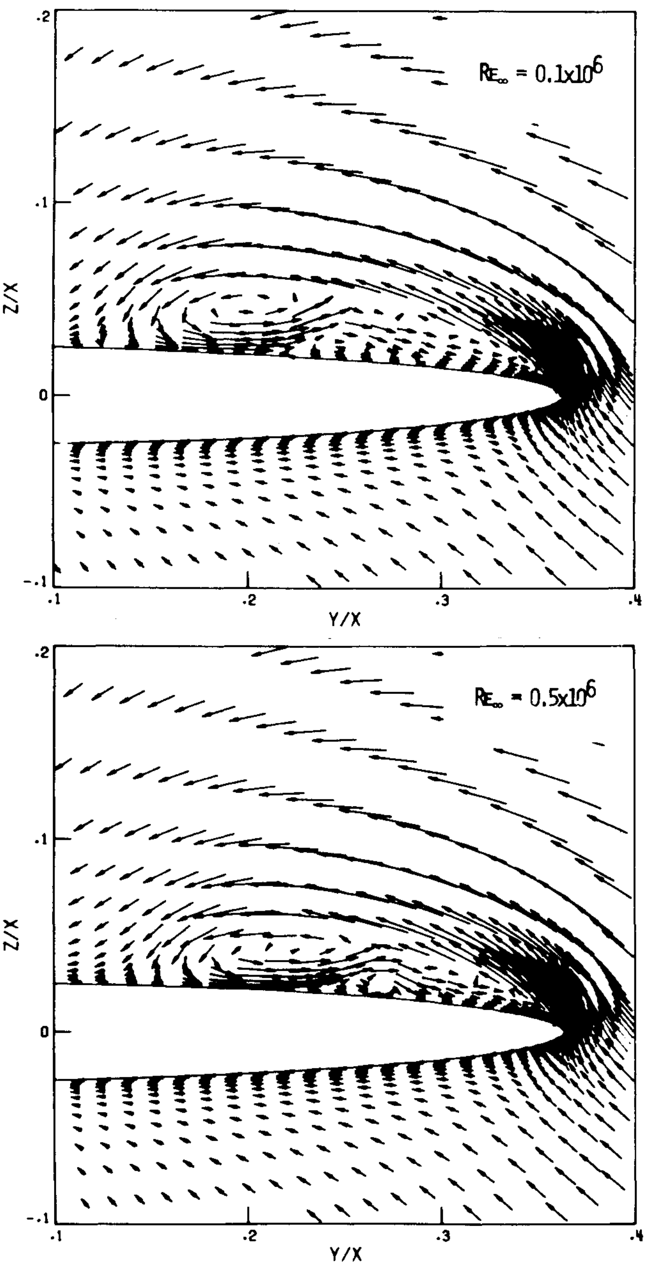

Fig. 4 Cross-flow velocity vectors, conical Navier-Stokes.

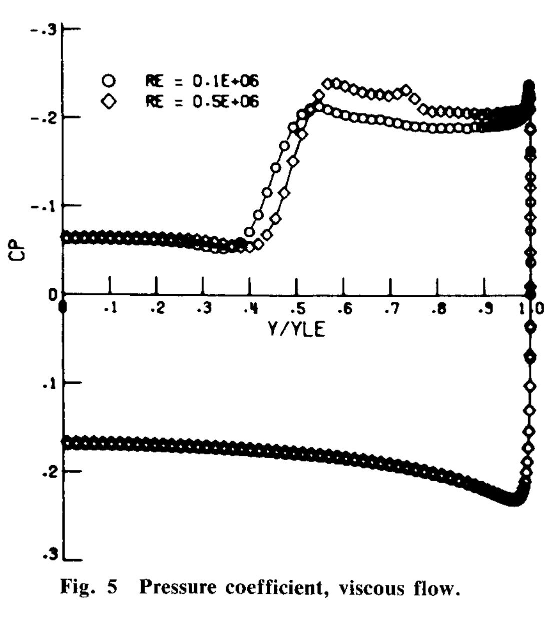

Fig. 5 Pressure coefficient, viscous flow.

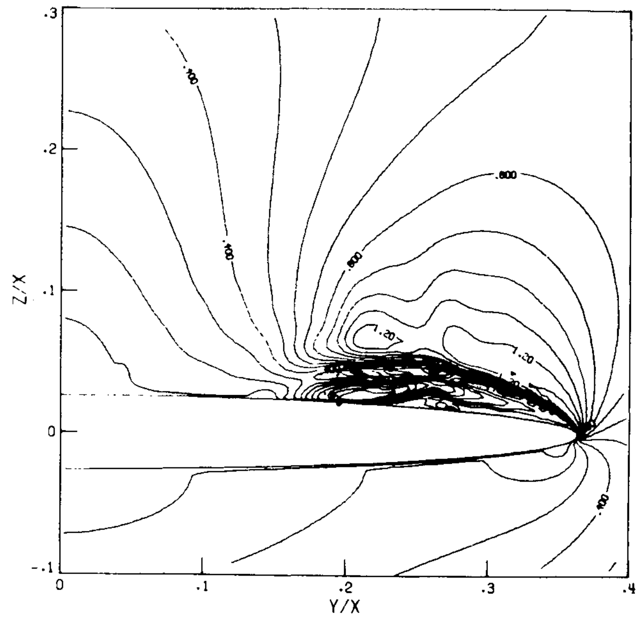

Fig. 6 Cross-flow Mach number, viscous flow, $Re_\infty = 0.5 \times 10^6$.

grid. The cross-flow velocity plot is given in Fig. 4. In general, the flow is quite similar to the previous case. The secondary vortex appears somewhat smaller relative to the primary vortex. A comparison of pressure coefficients, Fig. 5, shows the suction peak to be stronger for the higher Reynolds number. Cross-flow Mach number contours for the higher Reynolds number case are shown in Fig. 6. Although no experimental data were available for the case computed, an experimental study by Miller and Wood[25] for a flat delta wing with sharp beveled edges delineated seven different flow classifications according to the leading-edge Mach number and angle of attack. The computed results are in agreement with Miller and Wood's classification in which primary and secondary vortices are present and no cross-flow shock is observed. Subsequent to the publication of the paper from which this article is drawn, Squire[26] published experimental results for the 14:1 elliptic cone at different values of Mach and Reynolds numbers which are nevertheless quite similar to the present results.

Euler Solutions

The Euler solutions are characterized by the presence of vortical singularities in the symmetry plane on the upper and lower surfaces. The entire flow is weakly rotational inside the bow shock due to variable shock strength. Cross-flow streamlines terminate at either the upper or lower vortical singularity. Since each streamline crosses the bow shock at a different location, the entropy, density, and velocity at the singularities are multivalued. The dividing streamline terminates at the cross-flow stagnation point on the lower surface near the tip. On the body, the entropy propagates from this saddle point to the the vortical singularities. As a practical matter, for the present case, the bow shock is extremely weak and the entropy variation is negligible.

Inviscid solutions are presented for different grids, values of damping coefficients, and surface boundary conditions. The results were quite different.

Coarse Grid

Since a prime motivation in solving the Euler equations is the desire to avoid grid fineness necessary for viscous resolution, a coarse grid of (55×75) points was first considered. The minimum step size, $\Delta s/x = 0.005$, gives poor tip resolution, as can be seen in Fig. 7. Two different boundary conditions were investigated. The simplest boundary condition, extrapolation of the tangent velocity components, does not

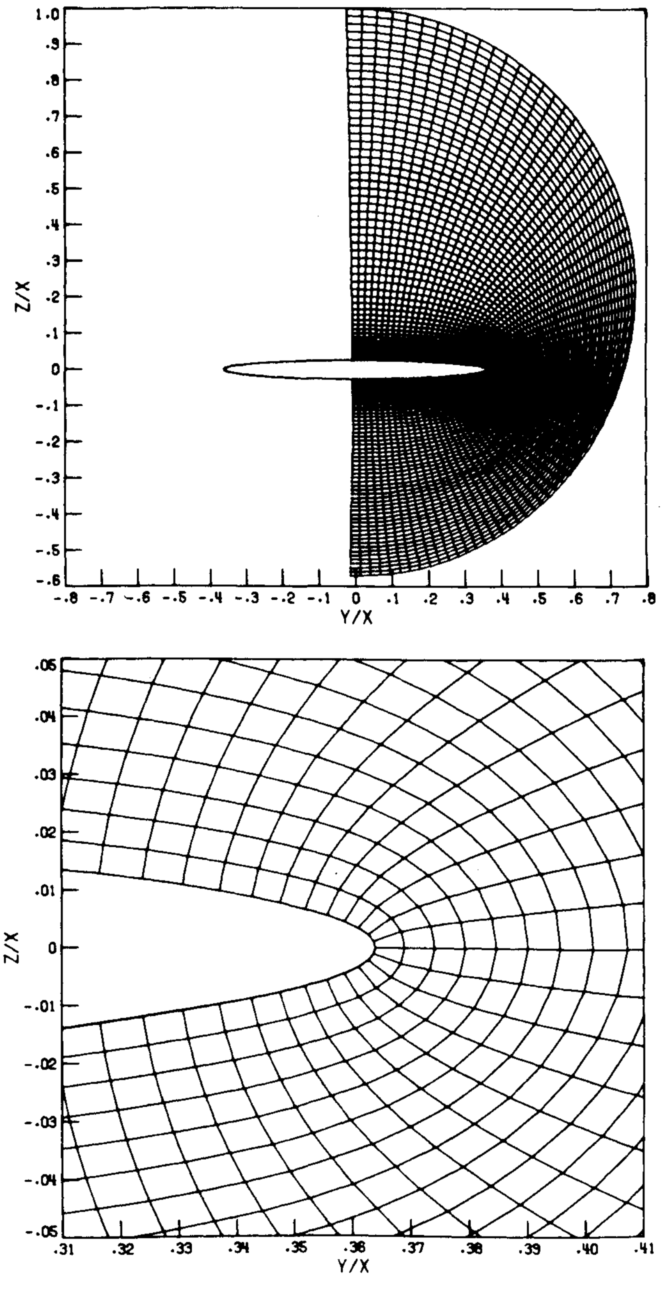

Fig. 7 Coarse-grid (75×55) points.

allow the rapid expansion at the tip to occur. This produces a viscous-like velocity defect in the cross-flow velocity profile. The Abbett boundary condition was also applied on the coarse grid. In this case, surface entropy must be specified. However, this is not known a priori, but evolves with the solution. As previously outlined, entropy is constant along streamlines except in crossing a shock. The propagation of entropy on the surface streamline results in the occurrence of a weak vortical layer that is not resolvable by the difference method. At best, it can be represented as a discontinuity between the surface and adjacent grid points. On the coarse grid considered, entropy production along streamlines due to numerical error completely overwhelms any effect of the vortical layer. It is then reasonable to simply ignore the vortical layer and extrapolate the surface entropy from neighboring interior points.

In Fig. 8, the pressure coefficient for the two inviscid boundary conditions is compared with the viscous result. The cross-flow velocity plot for the Abbett boundary condition is shown in Fig. 9. A comparison with the viscous result

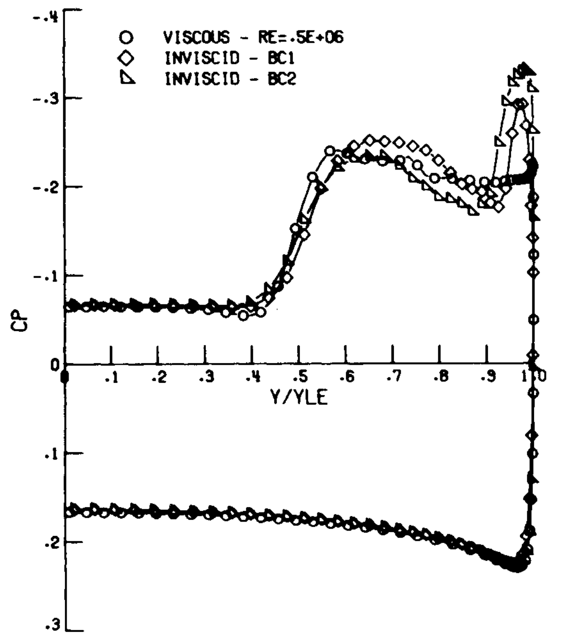

Fig. 8 Pressure coefficient, coarse-grid Euler vs fine-grid Navier-Stokes.

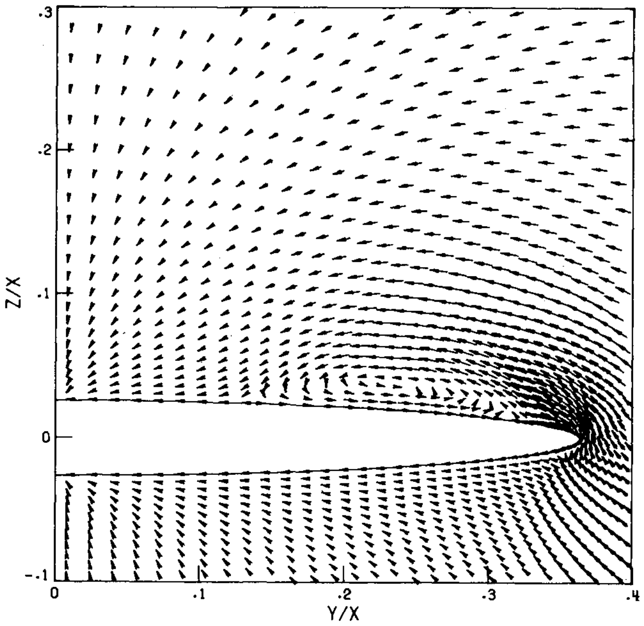

Fig. 9 Cross-flow velocity vectors, coarse-grid Euler, Abbett boundary condition (BC2).

in Fig. 4 reveals a large primary vortex of similar shape and size. Notably absent is the secondary vortex since there is no vorticity-generating mechanism on the upper wing surface. With the exception of the overexpansion at the leading edge, the inviscid pressure coefficients are in remarkable agreement with the viscous result. The Abbett boundary condition (BC2) recovers more of the inviscid expansion than the velocity extrapolation (BC1) but ultimately separates due to the generation of spurious entropy and vorticity at the leading edge. Separation occurs not at the leading edge, but at values of $y/y_{\mathrm{LE}} = 0.95$ (BC1) and 0.93 (BC2). The cross-flow Mach number and entropy contours for the Abbett boundary condition solution are shown in Fig. 10. The maximum entropy occurs at the tip and is convected through the vortex. The damping coefficient was varied parametrically over its range of stability for the Abbett boundary condition.

Surprisingly, the solution was relatively insensitive to the magnitude of the damping term. In order to maintain numerical stability, a time-accurate temporal resolution was required. For the lowest value of damping coefficient, instability was encountered unless the time step was further restricted to a value $\Delta t \approx 0.5 \Delta t_{\rm CFL}$.

Since the coarse-grid Euler solutions were time-accurate, the transient development of the vortex was observed. From the initial condition, the flow quickly expanded about the leading edge to a supersonic cross flow. A cross-flow shock also developed on the leeward surface with no separation evident. Concurrently, the leading-edge expansion produced large entropy/vorticity errors that were convected downstream to the developing cross-flow shock. The interaction of the two produced a separated region at the base of the shock. The separation then expanded to form the large primary vortex with the cross-flow shock largely absent in the steady state. However, referring to Fig. 10, a very small cross-flow shock adjacent to the surface at the point of separation, ($y/y_{\rm LE} = 0.93$), remains at steady state. Since the flow does not separate tangential to the body at the leading edge, the shock is the only mechanism by which the cross-flow velocity can switch, at the point of separation, from supersonic velocities of opposite sign. As the degree of numerical error at the tip increases, the point of separation moves closer to the leading edge and this shock need not be present. This transient sequence of events closely resembles those described in Ref. 14 with one important exception: the origin of the vorticity necessary for inviscid separation is numerical error at the leading edge and not the cross-flow shock.

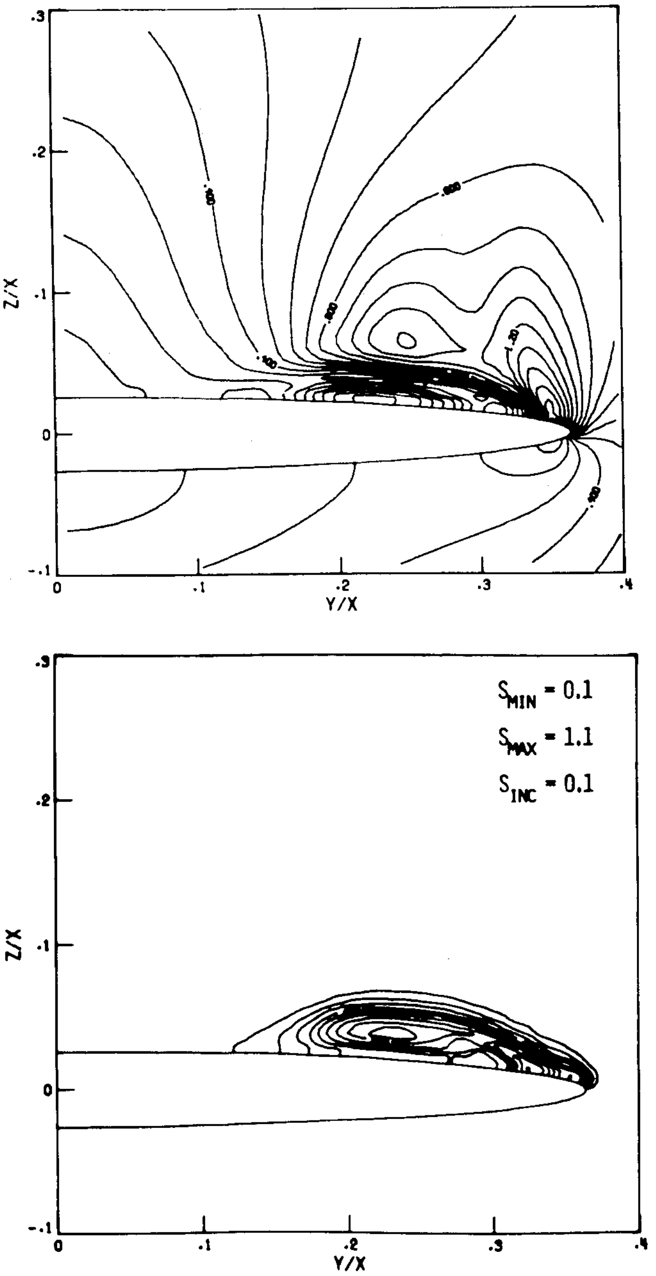

Fig. 10 Cross-flow Mach number and entropy contours, coarse-grid Euler.

Fine Grid

The finest grid used for the viscous solution, Fig. 3, was also used for the inviscid calculation. The intent was to reduce the effect of numerical error through better resolution of the tip region. Abbett's boundary condition was again applied with the entropy layer ignored. To further decrease unwanted dissipation, a switch was built into the code to smoothly turn the artificial damping off in the tip region. To remove any possible question of convergence, the residual was reduced nearly five orders of magnitude. It was expected that, with sufficient resolution, the leading-edge separation could be eliminated. This was indeed the case. Mildly surprising, however, was the occurrence of a small vortex well downstream of the cross-flow shock which is present in the absence of leading-edge separation. It will be demonstrated that this vortex is due to shock-generated vorticity and the calculation is a valid Euler solution. The pressure coefficient for this case is shown in Fig. 11. The result is very similar to the modified potential solution of Fig. 2. The full isentropic expansion is recovered, followed by recompression and the cross-flow shock. The modified potential approach is irrotational and does not exhibit the bump found in the Euler result at $y/y_{\rm LE} \approx 0.3$. Reference to the cross-flow velocity plot, Fig. 12, shows that the bump corresponds to a small vortex at $y/x \approx 0.1$. More importantly, the leading-edge separation is entirely absent. An enlarged view of the vortex, Fig. 12, provides some insight into its origin where a wake can be seen above the surface to the right of the vortex. A plot of the velocity profile at the cross-flow shock, Fig. 13, shows that this wake is generated by shock curvature. It should be noted that the preshock cross-flow velocity pro-

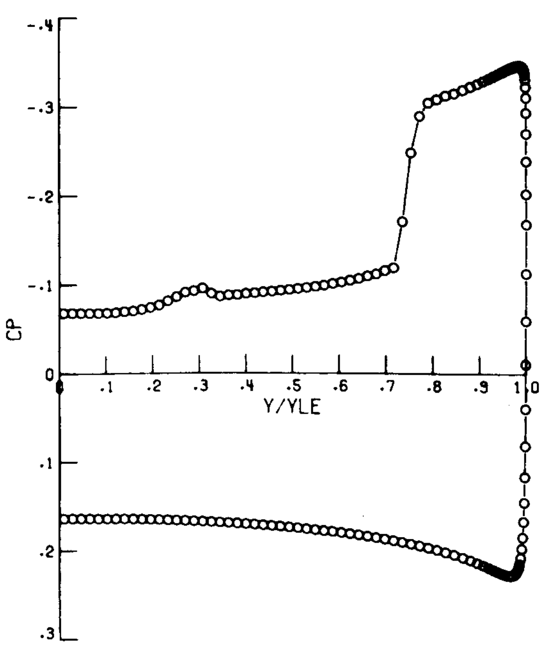

Fig. 11 Pressure coefficient, fine-grid Euler.

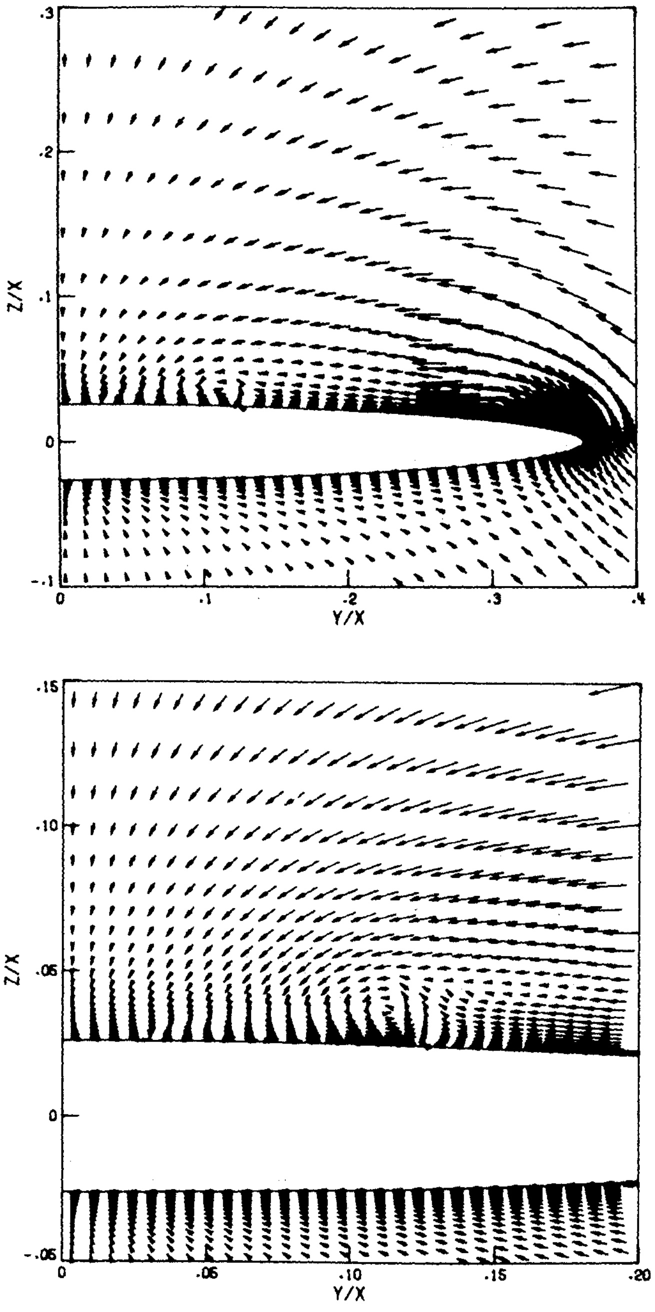

Fig. 12 Cross-flow velocity vectors, fine-grid Euler.

files do not show any sign of the viscous-like velocity defect found at the surface on the coarse grid due to inadequate leading-edge resolution. It is then safe to conclude that the shock is not being influenced by the tip region. In fact, the cross-flow velocity is very uniform near the wall and significant shock curvature does not occur until some 15 points away from the body. This is in contrast to the circular cone[13] where maximum shock strength and curvature occur at the body surface. A plot of the cross-flow Mach contours, Fig. 14, shows both the cross-flow shock and the shock-induced wake. In Fig. 15, enlarged views of the cross-flow Mach number and entropy contours are given. Entropy is generated across the shock according to the local shock strength. It is the entropy variation normal to the streamlines that produces the vorticity as required by Crocco's theorem and the subsequent vortex. Entropy generation at the tip has been reduced by over a factor of 20 relative to the coarse-grid calculation.

The fine-grid Euler solution was also computed with the correct entropy boundary condition. Entropy convection on the body is governed by the equation

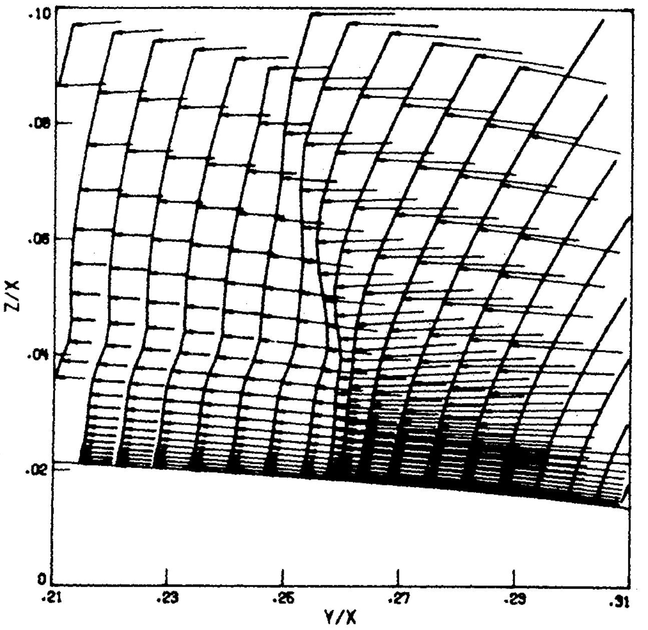

Fig. 13 Cross-flow velocity vector profile, fine-grid Euler.

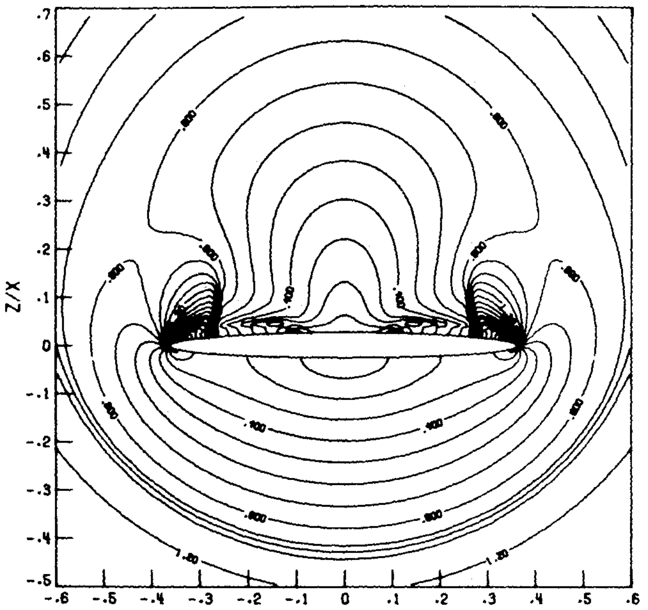

Fig. 14 Cross-flow Mach number contours, fine-grid Euler.

$$\frac{\partial s}{\partial t} + W\frac{\partial s}{\partial \eta} = 0$$

where W is the contravariant velocity along the body surface. At the cross-flow stagnation points (symmetry plane, windward tip, vortex reattachment point), entropy was extrapolated from the interior solution. The entropy jump across the (captured) cross-flow shock also was extrapolated from the interior solution. The entropy equation was then solved using windward differences to provide a new value of surface entropy for use by the Abbett scheme at the corrector level. In contrast with the simpler entropy extrapolation, the only difference observed was a small jump in entropy, density, and velocity magnitude on the body surface from the interior solution.

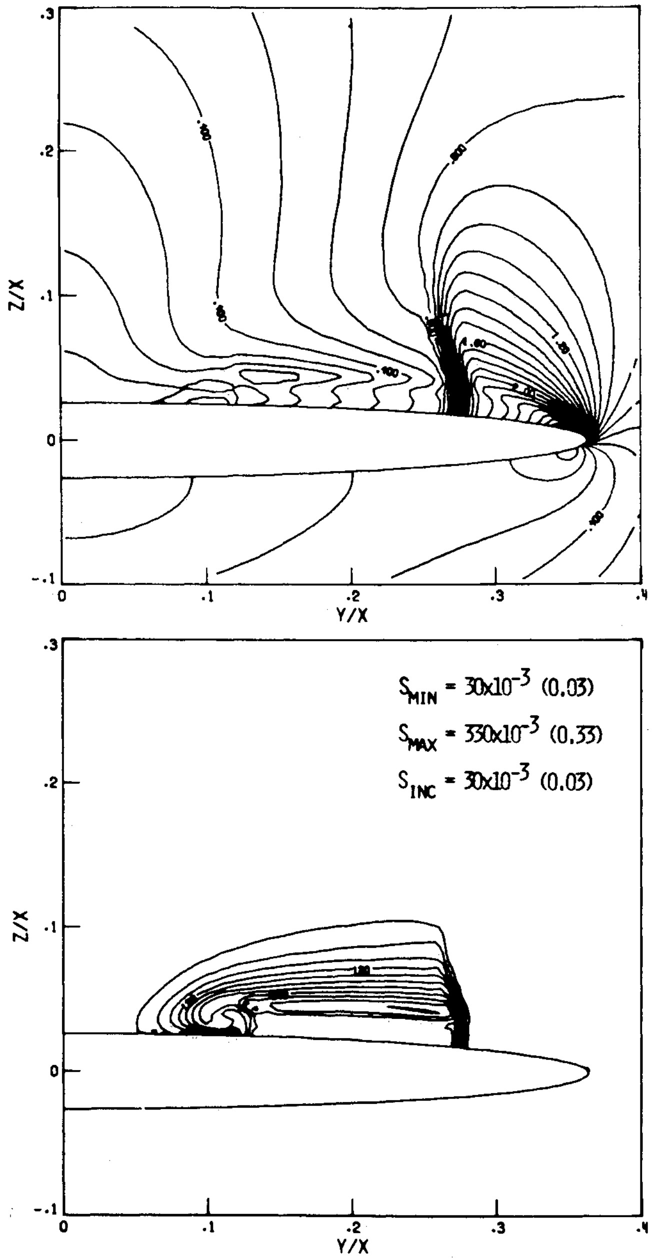

Fig. 15 Cross-flow Mach number and entropy contours, fine-grid Euler.

Kutta Condition

A limited investigation was made into the use of a Kutta condition to force separation to produce a grid-independent simulation of the actual viscous flow. The approach taken by Klopfer and Nielsen[27] was followed. The cross-flow velocity was set to zero, $W=0$, at the separation point computed by the viscous solution. Average values of pressure and density were specified at the separation point. Otherwise, the Abbett boundary condition procedure was applied as before. As a second alternative, the normal momentum equation, $\partial p/\partial N=0$, was used to specify the surface pressure, since there was no centripetal acceleration term at the stagnation point. This produced no significant change from the first condition. The Kutta condition was applied to previously computed coarse- and fine-grid Euler solutions. When applied to the coarse grid, the Kutta condition was ineffective in changing the point of separation from the numerically induced point of separation to the desired viscous location closer to the leading edge. The Kutta condition was also applied to the fine-grid Euler solution where the leading-edge separation had been eliminated. In order to ensure stability with the application of this boundary condition, a time-accurate path was followed. Here the Kutta condition specified the desired separation point correctly. The transient sequence of events included the convection of entropy/vorticity from the separation point to the cross-flow shock, separation at the base of the shock, growth of the separation to form a large primary vortex, and finally the disappearance of the shock-induced vortex. Plots of the cross-flow velocity vectors and Mach contours are given in Figs. 16 and 17. In this case, a weak cross-flow shock is apparent above the vortex near reattachment. The pressure coefficient is compared with the viscous result in Fig. 18. A sharp spike is evident at the leading edge since the inviscid flow expanded well beyond the viscous flow before the Kutta condition was encountered. In addition, the expansion in the vortex is

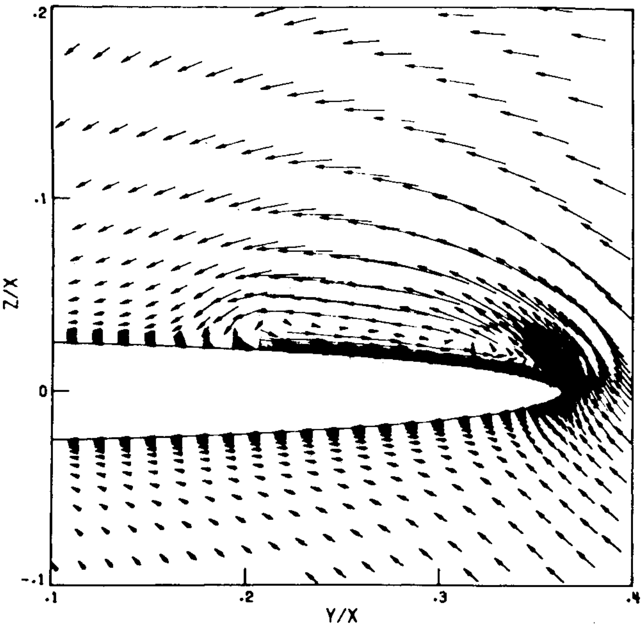

Fig. 16 Cross-flow velocity vectors, Kutta condition, fine-grid Euler.

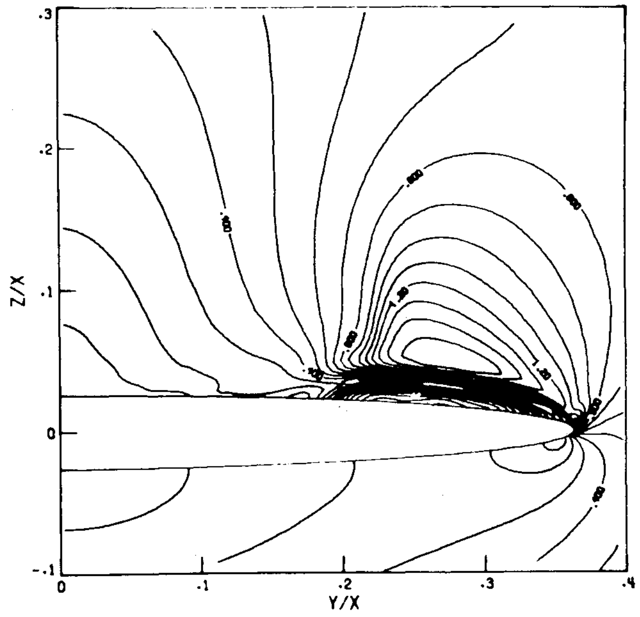

Fig. 17 Cross-flow Mach number contours, Kutta condition, fine-grid Euler.

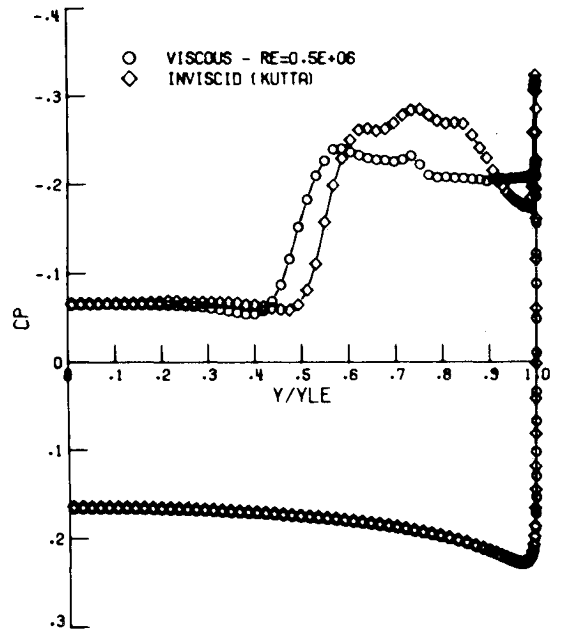

Fig. 18 Pressure coefficient, Kutta condition, fine-grid Euler.

significantly overpredicted compared to both the viscous and coarse-grid Euler results.

Conclusions

The Navier-Stokes and Euler equations were solved for the conical flow about a thin elliptic cone at a Mach number of 2 and a 10-deg angle of attack. The Navier-Stokes equations produced a leading-edge separation with a primary and secondary vortex on the leeward surface. Several Euler solutions were computed with very different results. On a coarse grid the flow resembled the viscous case, with a primary vortex and no secondary vortex. On a much finer grid, the leading-edge separation was eliminated and cross-flow, shock-induced vorticity produced a much smaller vortex near the symmetry plane. The following conclusions can be drawn for the present case:

1) The inviscid separation mechanism about the rounded leading-edge results from the spurious production of entropy and vorticity due to numerical error. Dissipative errors are introduced by the numerical algorithm and the artificial damping to control shock oscillations. However, for the present second-order method, the leading truncation error term is dispersive. Changes in grid resolution most dramatically affect the degree of error. To a lesser extent, artificial damping and inaccurate boundary condition implementation are further sources of error.

2) The use of the Euler equations to simulate viscous separation for flow about wings with rounded leading edges is not a consistent and reliable prediction method.

3) The application of a Kutta condition for the present case did not produce a grid-independent simulation of the viscous flow.

Acknowledgments

The author wishes to thank Dr. D. L. Dwoyer of the Computational Methods branch and Mr. M. D. Salas of the Theoretical Aerodynamics Branch for enlightening discussions on inviscid separation.

References

[1] Polhamus, E. C., "A Concept of the Vortex Lift of Sharp-Edged Delta Wings Based on a Leading Edge Suction Analogy," NASA TN D-3767, 1976.

[2] Johnson, T. T., Tinoco, E. N., Lu, P., and Epton, M. A., "Recent Advances in the Solution of Three-Dimensional Flows Over Wings with Leading Edge Separation," AIAA Paper 79-0282, Jan. 1979.

[3] Vigneron, Y. C., Rakich, J. V., and Tannehill, J. C., "Calculation of Supersonic Viscous Flow over Delta Wings with Sharp Subsonic Leading Edges," AIAA Paper 78-1137, July 1978.

[4] Fujii, K. and Kutler, P., "Numerical Simulation of the Leading Edge Separation Vortex for a Wing and Strake-Wing Configuration," *Proceedings of the AIAA Computational Fluid Dynamics Conference*, July 1983, pp. 567-583.

[5] Fijii, K. and Kutler, P., "Numerical Simulation of the Viscous Flow Over Three-Dimensional Complicated Geometries," AIAA Paper 84-1550, June 1984.

[6] Rizzetta, D. P. and Shang, J. S., "Numerical Simulation of Leading Edge Vortex Flows," AIAA Paper 84-1544, June 1984.

[7] Jameson, A., Schmidt, W., and Turkel, E., "Numerical Solutions of the Euler Equations by Finite Volume Methods Using Runge-Kutta Time Stepping Schemes," AIAA Paper 81-1259, June 1981.

[8] Hitzel, S. M. and Schmidt, W., "Slender Wings with Leading-Edge Vortex Separation—A Challenge for Panel Methods and Euler Codes," AIAA Paper 83-0562, Jan. 1983.

[9] Rizzi, A., Eriksson, L. E., Schmidt, W., and Hitzel, S. M., "Simulating Vortex Flows Around Wings. Aerodynamics of Vortical Type Flows in Three Dimensions," AGARD CP 342, 1983.

[10] Raj, P. and Sikora, J., "Free Vortex Flows: Recent Encounters with an Euler Code," AIAA Paper 84-0135, Jan. 1984.

[11] Manie, F., Neron, M., and Schmitt, V., "Experimental and Computational Investigation of the Vortex Flow Over a Swept Wing," *Proceedings, 14th Congress of the International Council of the Aeronautical Sciences*, ICAS-84-2.8.1, Sept. 1984, pp. 1-15.

[12] Salas, M. D., "Recent Developments in Transonic Euler Flow Over a Circular Cylinder," *Mathematics and Computers in Simulation XXV*, 1983, pp. 232-236.

[13] Marconi, F., "The Spiral Singularity in the Supersonic Inviscid Flow Over a Cone," AIAA Paper 84-0135, Jan. 1984.

[14] Rizzi, A., "Damped Euler-Equation Method to Compute Transonic Flow Around Wing-Body Combinations," *AIAA Journal*, Vol. 20, Oct. 1982, pp. 1321-1328.

[15] Barton, J. T. and Pulliam, T. H., "Airfoil Computations at High Angles of Attack, Inviscid and Viscous Phenomena," AIAA Paper 84-0524, Jan. 1984.

[16] McRae, D. S., "A Numerical Study of Supersonic Viscous Cone Flow at High Angle of Attack," AIAA Paper 76-97, Jan. 1976.

[17] Bluford, G. S., "Numerical Solution of the Supersonic and Hypersonic Viscous Flow Around Thin Delta Wings," *AIAA Journal*, Vol. 17, Sept. 1978, pp. 942-949.

[18] MacCormack, R. W., "Numerical Solutions of the Interactions of a Shock Wave with a Laminar Boundary Layer," *Lecture Notes in Physics*, Vol. 8, Springer-Verlag, New York, 1971, pp. 151-163.

[19] MacCormack, R. W. and Baldwin, B. S., "A Numerical Method for Solving the Navier-Stokes Equations with Application to Shock-Boundary Layer Interactions," AIAA Paper 75-1, Jan. 1975.

[20] Warming, R. F. and Hyett, B. J., "The Modified Equation Approach to the Stability and Accuracy Analysis of Finite Difference Methods," *Journal of Computational Physics*, Vol. 14, 1974, pp. 159-179.

[21] Abbett, M. J., "Boundary Condition Computational Procedures for Inviscid Supersonic Flow Field Calculations," Aerotherm Corp., Mt. View, CA, Final Rept. 71-41, 1971.

[22] Grossman, B., "Numerical Procedure for the Computation of Irrotational Conical Flows," *AIAA Journal*, Vol. 17, Aug. 1979, pp. 828-837.

[23] Bradley, P. F., Dwoyer, D. L., South, J. C., and Keen, J. M., "Vectorized Schemes for Using the Artificial Density Method," AIAA Paper 84-0162, Jan. 1984.

[24] Siclari, M. J. and Rubel, A., "Entropy Corrections to Supersonic Conical Nonlinear Potential Flows," AIAA Paper 84-1683, June 1984.

[25] Miller, D. S. and Wood, R. M., "An Investigation of Wing Leading-Edge Vortices at Supersonic Speeds," AIAA Paper 83-1816, July 1983.

[26] Squire, L. C., "Leading-Edge Separation and Crossflow Shocks on Delta Wings," *AIAA Journal*, Vol. 23, March 1985, pp. 321-325.

[27] Klopfer, G. H. and Nielsen, J. N., "Euler Solutions for Wing and Wing-Body Combination at Supersonic Speeds with Leading-Edge Separation," AIAA Paper 80-0126, Jan. 1980.